Atmos. Chem. Phys. Discuss., 15, 18109–18149, 2015
www.atmos-chem-phys-discuss.net/15/18109/2015/
doi:10.5194/acpd-15-18109-2015

Atmospheric Chemistry and Physics Discussions

Aerosol size distribution seasonal characteristics measured in Tiksi, Russian Arctic

E. Asmi[1], V. Kondratyev[1,2], D. Brus[1], T. Laurila[1], H. Lihavainen[1], J. Backman[1], V. Vakkari[1], M. Aurela[1], J. Hatakka[1], Y. Viisanen[1], T. Uttal[3], V. Ivakhov[4], and A. Makshtas[5]

[1]Atmospheric Composition Research, Finnish Meteorological Institute, Helsinki, Finland
[2]Yakutian service for hydrometeorology and environmental monitoring, Tiksi branch, Russia
[3]National Oceanic and Atmospheric Administration, Boulder, USA
[4]Voeikov Main Geophysical Observatory, St. Petersburg, Russia
[5]Arctic and Antarctic Research Institute, St. Petersburg, Russia

Received: 01 June 2015 – Accepted: 16 June 2015 – Published: 02 July 2015

Correspondence to: E. Asmi (eija.asmi@fmi.fi)

Published by Copernicus Publications on behalf of the European Geosciences Union.

Abstract

Four years of continuous aerosol number size distribution measurements from an Arctic Climate Observatory in Tiksi Russia are analyzed. Source region effects on particle modal features, and number and mass concentrations are presented for different seasons. The monthly median total aerosol number concentration in Tiksi ranges from 184 cm^{-3} in November to 724 cm^{-3} in July with a local maximum in March of 481 cm^{-3}. The total mass concentration has a distinct maximum in February–March of 1.72–2.38 $\mu g\,m^{-3}$ and two minimums in June of 0.42 $\mu g\,m^{-3}$ and in September–October of 0.36–0.57 $\mu g\,m^{-3}$. These seasonal cycles in number and mass concentrations are related to isolated aerosol sources such as Arctic haze in early spring which increases accumulation and coarse mode numbers, and biogenic emissions in summer which affects the smaller, nucleation and Aitken mode particles. The impact of temperature dependent natural emissions on aerosol and cloud condensation nuclei numbers was significant. Therefore, in addition to the precursor emissions of biogenic volatile organic compounds, the frequent Siberian forest fires, although far are suggested to play a role in Arctic aerosol composition during the warmest months. During calm and cold months aerosol concentrations were occasionally increased by nearby aerosol sources in trapping inversions. These results provide valuable information on inter-annual cycles and sources of Arctic aerosols.

1 Introduction

The Arctic and northern boreal regions of Eurasia are changing rapidly as a consequence of increased human activities (Richter-Menge et al., 2006; Bond et al., 2013). Aerosol particles are one of the major climate forcers in the Arctic; they reflect and absorb incoming solar radiation, modify the properties of clouds and affect the surface albedo. Shindell and Faluvegi (2009) suggested that over two thirds of the observed

ACPD
15, 18109–18149, 2015

Arctic surface temperature increase during the last decades is attributed to changes in concentrations of sulphate and black carbon (BC) aerosols.

Aerosol particles on snow and ice-covered regions have specific climate impacts and feedback processes. Recent experimental evidence indicates that in pristine polar regions the aerosol-cloud feedback can be extremely sensitive to aerosol numbers (Asmi et al., 2012), and that Arctic clouds, contrary to those occurring at lower latitudes, can enhance overall warming of the surface (Walsh and Chapman, 1998; Mauritsen et al., 2011). To understand these processes, information on aerosol sizes is of particular interest, however, only a few long-term studies of aerosol number and size distributions from the Arctic locations exist (Bodhaine, 1989; Tunved et al., 2013). These have suggested a rather clear seasonal cycle of increased particle number and mass in early spring as a consequence of the Arctic Haze phenomena (Mitchell, 1957). Currently, commonly used global and chemical transport models consistently fail in predicting Arctic aerosol seasonal cycles, and also encounter problems in capturing the composition and quantities of polar aerosols (Bourgeois and Bey, 2011; Liu et al., 2012; Bond et al., 2013). Several studies suggest that this can be attributed to problems in treatment of aerosol transport in models, and in particular in wet scavenging processes (e.g., Liu et al., 2012). Some recent studies also indicate that a number of sources have been neglected (Hienola et al., 2013; Stohl et al., 2013; Stock et al., 2014).

South of the Arctic in the Eurasian side is the vast Siberian region from which knowledge of aerosol properties is particularly limited. Recently, some studies documenting interannual variability of aerosol distributions from central Siberia were published revealing the importance of Siberian boreal emissions on aerosol number and mass distributions (Heintzenberg et al., 2008, 2011; Chi et al., 2013). The impact of forest emissions on aerosol numbers and mass, and the temperature related feedback connected with these emissions, is suggested by previous studies from other regions (Tunved et al., 2006; Asmi et al., 2011; Paasonen et al., 2013); however, the relative importance of biogenic emissions for aerosols in the current and future warming Arctic is still an open question.

ACPD
15, 18109–18149, 2015

In this work, to fulfill these observational data gaps, we present long-term, high-quality observations from Arctic Siberia by introducing four years of continuous aerosol number size distribution observations from the Tiksi Hydrometeorological Observatory. We will quantify aerosol modal features, number and mass concentrations and analyze their temporal evolution in terms of source region controls and local weather parameters. Our goal is to assess the importance of Siberian boreal regions biogenic and wild fires emissions, the build-up of the Arctic haze, and that of possible local emissions for the observed aerosol numbers, mass and their climatically relevant properties. Analysis of the nucleation mode aerosols will also elucidate the potential of secondary sources to produce particles under different conditions in the Arctic.

2 Methods

2.1 Site description

History and a general overview of Tiksi International Hydrometeorological Observatory is fully described in Uttal et al. (2013). Tiksi meteorological observatory in northern Siberia 71°36′ N; 128°53′ E) on the shore of the Laptev Sea has been operating since 1930s. As an International Polar Year (IPY) 2007–2008 activity, the observatory was further upgraded and joined in the network of the International Arctic Systems for Observing the Atmosphere (IASOA, www.IASOA.org). The Tiksi observatory is run in collaboration between NOAA (National Oceanic and Atmospheric Administration) with the support of the NSF (National Science Foundation), Roshydromet AARI (Arctic and Antarctic Research Institute) and MGO (The Voeikov Main Geophysical Observatory) units, Yakutian service for hydrometeorology and environmental monitoring, and the FMI (Finnish Meteorological Institute). FMI activities in Tiksi were initiated in summer 2010 and include aerosol number size distribution measurements presented here.

The city of Tiksi is on the Lena river delta with current population of about 5000 inhabitants. Meteorological observatory is located 5 km further down to south-west from

ACPD
15, 18109–18149, 2015

the city, separated by a hill, and is about 500 m distance from the coast of the Laptev sea (Fig. 1). Airport of Tiksi is further up north from the city and the station. The site is well above the treeline and is surrounded by low tundra vegetation and a line of mountains in the south.

2.2 Measurements

Measurements of aerosol size distributions, along with many other atmospheric parameters (for these, see Uttal et al., 2013), were started in 05 July 2010. Aerosol number size distribution from 7 to 500 nm (later on from 3 to 800 nm) is measured with a twin-Differential Mobility Particle Sizer (DMPS) system and the distribution up from 500 nm with an Aerodynamic Particle Sizer (APS model 3321, TSI Inc., USA). For further description of the instruments, see Sect. 2.2.1. Time resolution of DMPS measurements is set to 10 min and APS to 5 min.

Both of the instruments are attached to an inlet line tube, which is of diameter of 16 mm. The tube is fixed just above the instrument rack and extending 2 m above the roof of the building and 6.5 m above the ground. The APS inlet is direct from the roof, with a length of 2.5 m. The DMPS inlet length is 4–5 m, and the theoretical diffusional losses during the particle transport are taken into account in the data inversion.

The inlet tube is equipped with an inlet head of a fixed cut-off size of 10 µm (BGI Inc, USA). The head also protects the instruments from snow, rain and soil contaminants. Flow through the inlet is kept at a constant $1\,m^3\,h^{-1}$ with an additional compensating flow, regulated depending on the total flow of all instruments. For example, when aethalometer with a flow-rate of $5\,L\,min^{-1}$ was added on line with the DMPS and APS in August 2010, the compensating flow was reduced from 10 to $5\,L\,min^{-1}$. Heating (self-regulating) and isolation were added on the inlet tube in summer 2012, after two winters of relatively poor data coverage due to icing problems.

Flows and proper operation of all instruments are fully checked twice per year during the station maintenance visits. Additionally, the automated flow, temperature and pressure sensors allow the control of instruments and data over the span of the year. The

ACPD
15, 18109–18149, 2015

station staff is trained to solve problems which might occur unexpectedly and they are also in charge of the regular maintenance done weekly.

Data is transferred real-time to AARI via satellite connection and daily to NOAA and FMI servers, and quality checked weekly.

2.2.1 Size distributions

The twin-Differential Mobility Particle Sizer (DMPS) system used in Tiksi since 2010, as well as our data inversion procedure, are thoroughly described in Wiedensohler et al. (2012) and here only a brief summary is given.

The twin-DMPS consists of two identical DMPS systems: one equipped with a short Vienna-type DMA to measure particle sizes from 7 to 115 nm and one with a medium-long Vienna-type DMA to measure particle sizes from 15 to 500 nm. Both use a condensation particle counter (CPC model 3772, TSI Inc., USA) as a particle detector. DMPS sheath flows are controlled by a blower (Ametek, USA) and regulated with a PID-controller. Aerosol flow rate of 1 $\mathrm{L\,min^{-1}}$ and sheath flow rate of 6 $\mathrm{L\,min^{-1}}$ are used. The size range of DMPS measurements was extended up to 800 nm in 15 May 2012. Further extension of the measurement size range down to 3 nm was done in 03 July 2013, when the original CPC model 3772 was replaced with a CPC model 3776. The CPC 3772 was then installed to measure the particle total number concentration. Flows of the short-DMPS system after this are 1.5 and 9 $\mathrm{L\,min^{-1}}$, for aerosol and sheath respectively. Dryer is not used in front of the instruments since the sample air RH remains close to zero during majority of the year, with the maximum measured so far being 30 %.

2.2.2 Auxiliary weather parameters

Air temperature and relative humidity are measured by Vaisala HMP45D Pt100 and capacitive sensors. Solar radiation is monitored by Kipp&Zonen CMP3 pyranometer and air pressure by Vaisala PMT16A attached to Vaisala QML201 data logger. Metek USA-

ACPD
15, 18109–18149, 2015

1 sonic anemometer is used for wind and turbulence observations. Up to July 2013, we used auxiliary meteorological data measured at the micrometeorological flux cabin located 250 m to the south from station building. Beginning on 09 July 2013 auxiliary data are from the station. In this new location, wind is observed at a 10 m tower instead of the earlier 3 m flux measurement mast.

2.3 Data analysis

All the data are measured and presented in UTC time. The solar midday in Tiksi is around 13:30 LT (22:30 in UTC). No conversion to STP was done, since the site is at a sea level and measurement temperature remains relatively stable around 20 °C.

2.3.1 Data coverage

Due to harsh winter conditions and remoteness of the Tiksi site, in addition to instrument related failures, some of the data were lost in particular during the first two winters (Fig. S1, in the Supplement). The overall data coverage in our DMPS measurements was 74 %, but additional 36 % of those were lost in data cleaning. The data coverage for APS was 30 %, and for meteorological (T, RH, Winds and Radiation) measurements it was 76 %.

2.3.2 DMPS data inversion, cleaning and quality checking

DMPS data were inverted using measured flow rates and the default temperature of 293 K and a pressure of 1 atm, using the routine as described in Wiedensohler et al. (2012). Briefly, the data inversion routine uses the charging probabilities defined by Wiedensohler (1989), the transfer functions of Stolzenburg (1988) and takes into account the theoretical diffusion losses of particles in measurement lines and inside the DMAs, as well as accounts for the calibrated CPC detection efficiencies.

As a first step, all data were inverted and manually checked for any instrument or inversion related failures. This data is here referred as all the data available. As a sec-

ACPD
15, 18109–18149, 2015

ond step, this data was cleaned from any local pollution, which was mainly related with activities in Tiksi city north from the station. Therefore, the wind direction and speed were used as an indication and all data during winds from sector 315–45° were removed, as well as those values measured with wind speeds $< 1\,\mathrm{m\,s^{-1}}$. In addition to this, occasional short-term peaks, especially when occurring in Aitken mode sizes, were removed. These peaks might have been caused by variable human activities in the vicinity of the station, for example the personnel transportation to the station using motor vehicles.

For the period of about 10 months (03 July 2013–14 May 2014) of coincident DMPS and CPC measurements, the quality of data and that of the DMPS inversion routine was additionally verified by making a comparison of the DMPS total integrated number (in a size range of 7–500 nm) and the total number measured by the CPC 3772. A median of CPC number during the size-stepping period of 10 min of the overlapping DMPS measurements was used in comparison. A least-square-fit of DMPS vs. CPC number as constrained with a zero-intercept forcing, resulted in a slope of 0.98 with a coefficient of determination, R-squared, value of 0.92.

2.3.3 Diameter and density correction to APS

The APS measures the aerodynamic particle sizes while the DMPS measures the particle mobility (equals geometric, assuming a shape factor of one) sizes. The aerodynamic diameters of particles (D_a) are related to mobility diameters

$$D_p = D_a \sqrt{\frac{\rho_0}{\rho_p}} \sqrt{\frac{C_c(D_p)}{C_c(D_a)}}, \quad (1)$$

where ρ_0 is the density of D_a, in this case the unit density of a sphere ($1\,\mathrm{g\,cm^{-3}}$), and ρ_p is the density of D_p. The square-root of the ratio of the slip correction terms (C_c) can be approximated as unity here, since the underestimation due to this is very minor at the size range of question, $D_p > 500$ nm.

ACPD
15, 18109–18149, 2015

To combine our observations we still need to approximate the particle density ρ_p. As a first approximation, we used a value of 1.5 g cm^{-3}, previously reported and largely used for northern Finland boreal forest site (Saarikoski et al., 2005; Viskari et al., 2012). The goodness of this approximation was also tested by matching the APS and DMPS data from the period of overlapping measurements, 16 January–26 November 2013. The APS data was merged with the time frame of the available DMPS measurements using averaging when several APS observations were available from the 10 min period of DMPS measurement cycle. Furthermore, the highest and the lowest 10th percentiles (based on total concentration) were removed from both the DMPS and APS data, leaving 66 % of the overlapping data available for the analysis. The density correction to APS changed the lowest measured diameter size from 500 to 410 nm.

The APS showed lower concentrations at the size range where the instruments overlap (Fig. S2, in the Supplement). It is likely that the APS under-counts the particles at its lowest channels, while the DMPS correspondingly suffers from larger statistical errors at its highest channels where the number concentrations are low. Therefore, the three lowest channels of the APS and the highest of the DMPS were discarded from the further analysis, leaving a comparison size range from 493 to 658 nm (lower and upper size limit). A scatter of these data yet resulted in a slope of 1.79 (R^2 = 0.56), the APS underestimating the particle concentration (Fig. S3, in the Supplement). The slope appeared to be slightly steeper in warm months (July–August), possibly indicating a decrease in particle density. However, since both of the instruments used are known to have troubles in their overlapping size range, further corrections (e.g. a correction of a detection efficiency) were not done and thus the coarse mode aerosol concentration derived based on APS data should be interpreted as a lower limit estimate. All the APS data shown here are presented in mobility diameters, assuming the particle density of 1.5 g cm^{-3}.

ACPD
15, 18109–18149, 2015

2.3.4 Calculation of air-mass back-trajectories

Air mass back trajectories at arrival levels of 100, 500 and 1000 m a.s.l. for Tiksi were calculated using a HYSPLIT 4 model (Draxler and Hess, 1997, 1998; Draxler, 1999). The National Weather Service's National Centers for Environmental Prediction (NCEP) Global Data Assimilation System (GDAS) was used as a meteorological data input for the HYSPLIT model runs. A new trajectory was started every 3 h calculating 120 h backwards. Trajectories calculated for different arrival heights showed generally very similar paths and for example, the overall calculated average fraction of air masses over the continent was 0.70, 0.68 and 0.69 for 100, 500 and 1000 m heights, respectively.

2.3.5 Clustering of size distributions

Cluster analysis technique was applied to divide particle size distributions into eight (8) mutually different, but internally similar groups. K-means clustering algorithm, previously denoted as an efficient and well qualified method for clustering particle size distributions (Beddows et al., 2009), was used for minimizing the within cluster variance (sum of squared Euclidean distances from cluster centers). Number of clusters was chosen based on several test runs with different number of clusters. The initial cluster centroid positions for the iterative algorithm were chosen randomly, which however, based on several consecutive runs did not affect final cluster composition significantly.

3 Results

3.1 Seasonal cycles of meteorological variables

Meteorological conditions (Fig. 2) in Tiksi display large annual variability that is controlled by alternating periods of polar night (19 November–24 January) and the midnight sun (11 June–03 August). With respect to the variables analyzed (i.e. temperature, RH, radiation, winds and air mass origin), the years from 2010 to 2014 had similar seasonal

ACPD
15, 18109–18149, 2015

cycles. Median temperatures stayed above zero for four months each year between June and September. This period was also characterized by the highest frequency occurrence of marine air masses, highest absolute values and variability in relative humidity, and most stable wind speeds with median values extending from 3 to 5 $m\,s^{-1}$. A shift occurred in October with the sudden onset of decreased solar insolation resulting in temperature shift to below zero. RH decreases were correlated with decreasing temperature until January–February, after which the increasing solar radiation resulted in increasing temperature and RH. The cold month winds were primarily as continental with low frequency occurrence of marine air masses. In October through December, very high wind speeds occurred with half hour averages of up to 20 $m\,s^{-1}$ indicating stormy weather conditions. January through March was the calmest period of the year with median wind speeds between 1 and 3 $m\,s^{-1}$. A shift in weather conditions occurs in April–May with increasing temperatures and stronger winds and the onset of more frequent marine air flow. Precipitation data was examined from the Russian Roshydromet weather observations for years 2010–2014. During the analysis period, most precipitation occurred in July–August when the monthly average precipitation amounts were > 50 mm. The driest seasons were February–May and October–November when the monthly average precipitation was < 20 mm.

3.2 Number and mass size distributions modal characteristics

To study the impact of different environmental conditions on modal characteristics of aerosol size distributions, the quality controlled DMPS data (diameter range from 7 to 500 nm) were clustered into eight mutually dissimilar groups using the methodology explained in Sect. 2.3.5. A median of 1.5 h distributions were used in order to catch the typical features corresponding to different air mass types (3 h time resolution) as well as to variable meteorological parameters (0.5 h time resolution). To further elucidate the differences in spectral shapes of the distributions, each size distribution were normalized with its maximum concentration (Fig. 3a).

ACPD
15, 18109–18149, 2015

Clusters 1–3 have the highest average number concentrations with distinct Aitken modes and relatively weak accumulation modes. Of those three clusters, number 1 have the highest median number concentration (1138 cm^{-3}) and the largest peak mode diameter (72 nm). For clusters 2 and 3 the median number concentrations are 820 and 501 cm^{-3}, and peak mode diameters are 50 and 32 nm, respectively. This group of clusters appears to best represent summer time aerosol size distributions with different degrees of aerosol aging resulting from different passage times over continental Siberia with cluster 1 representing the most continental air mass and cluster 3 the least continental air mass. These clusters types occurred only occasionally in winter months.

Clusters 7 and 8 have distinct accumulation modes (Fig. 3a). These are the two most prevalent cluster types, occurring during 50 % of the measurement period and characterized by the lowest average number concentration of $< 400\,cm^{-3}$ (Table 1). Clusters 7 and 8 are the most common between November and May (Fig. S4, in the Supplement), which is also reflected in mean meteorological variables calculated for these clusters (Table 1).

The remaining three clusters: numbers 4–6, are predominantly marine and occured mainly in spring, summer and autumn months (Fig. S4, in the Supplement) with median number concentrations ranging from 257–366 cm^{-3}. In addition to marine characteristics, these clusters share bi-modal size distributions with strong nucleation modes, especially in clusters 5 and 6. Cluster 4 is more mixed with continental and aging characteristics that result in an increased peak diameter of the smaller mode to 40 nm. In contrast to clusters 1–3 where aging increase both the modal peak diameter and the particle number, in clusters 4–6 the modal peak diameter shifts from < 7 nm (Cluster 5), to 20 nm (Cluster 6) and up to 40 nm (Cluster 4), while the number concentrations decrease. This indicates a lack of additional sources and simultaneous marine aerosol aging processes such as coagulation and particle cloud processing.

The origin of the air masses corresponding to each of the clusters 1–8 are distributed between more southerly continental ones and more coastal or regional ones

ACPD
15, 18109–18149, 2015

(Fig. S5, in the Supplement). Clusters 1, 2, 7 and 8, are the most continentally influenced with mainly southerly air mass origins. Cluster 4 also commonly has air masses with southerly origins. The most marine cluster types: 3, 5 and 6 do not typically have air flows from south, but rather from nearby coastal regions that indicate mixing of both regional continental and marine influences.

Similar clustering analysis was done for normalized mass size distributions, with assumed particle density of 1.5 g cm^{-3} (Figs. 3b and S4, in the Supplement; Table 2). The results show a clear seasonal distinction. APS data were not used in clustering due to poor data coverage, however, the results for coarse mode (when available) are presented.

The highest total mass concentrations appear in clusters 1 and 2. These clusters were mainly observed during winter and early spring, thus possibly connected with Arctic haze and wintertime inversions of pollutants close to surface. Cluster 8 has lower concentrations typical of transition seasons when the polar vortex is forming or breaking up. Clusters 5 and 6 have the smallest total mass concentrations and are representative of marine air masses that occurred mainly during summer months. Cluster 7 is also clearly marine, but occurred in mid-winter and shows increased mass in the coarse mode, as measured by APS. The fourth somewhat marine cluster is number 4, which was common in early summer and late autumn, and shows an increased mass concentration in accumulation mode. In late autumn the possible influence of sea spray aerosols results in increased particle mass in this cluster. The remaining cluster 3 occurred in all seasons but was relatively rare except during mid-summer and late-winter. The unique feature of cluster 3 is high mass in Aitken mode sizes.

Based on these particle modal features, four modes: nucleation (7–25 nm), Aitken (25–100 nm), accumulation (100–500 nm) and coarse (> 410 nm from APS, when available), were identified; these are discussed in following sections.

ACPD
15, 18109–18149, 2015

3.3 Temporal variability of aerosol number and mass

Total particle number concentrations (Fig. 4a and Table 3) show two annual maxima in March and in July. A similar interannual cycle is seen for each particle mode separately, but with differing with magnitudes. For the nucleation and Aitken mode particles the July maxima are the highest whereas for the accumulation and coarse mode particles the March maxima are larger. The particle mass concentration maxima in March became even more dominant and persisted through the months of late winter and spring (Fig. 4b and Table 3). This indicates the significant influence of Arctic haze, which primarily increases the larger particle numbers and masses suggesting impacts via indirect aerosol effects and atmospheric visibility. Similar behavior can also be seen in seasonally cycles of size distributions where the Aitken mode is the most dominant only during June–August (Fig. S6, in the Supplement).

Compared to aerosol number size distributions measured in northern Finland at the Pallas and Värriö Arctic sites (Laakso et al., 2003; Tunved et al., 2003), the distributions in Tiksi show similar seasonal variability but with lower concentrations throughout the year. Instead, compared to measurements in more higher latitude Arctic sites at Barrow and Zeppelin the number concentration in Tiksi is higher especially during spring and summer (Bodhaine, 1989; Tunved et al., 2013). The mass concentrations in Tiksi presents a similar annual variability as those measured at Barrow and Zeppelin sites but a quantitative comparison between them is difficult due to different methods and size ranges used (Quinn et al., 2002; Tunved et al., 2013).

Nucleation mode particles are indicative of secondary production processes taking place in the Arctic. A clear minimum in nucleation mode concentration was observed in January with increases in concentration with the increasing seasonal solar radiation indicating a photochemically driven process. Despite the high particle mass during the Arctic haze period, secondary production of particles also appears to take place as soon as solar radiation is available. This is opposite to what is seen at the high-latitude Arctic sites Barrow and Zeppelin (Bodhaine, 1989; Tunved et al., 2013) but similar to

ACPD
15, 18109–18149, 2015

what is observed at a continental northern Finland Arctic site Pallas (Asmi et al., 2011). The origin of the nucleating and condensation vapors may therefore be connected with regional continental sources, in addition to what is contained in the haze itself. However, the long-range transported haze aerosols are also likely to be important for secondary particle formation and growth process since after the dissipation of Arctic haze later in the spring, the nucleation mode concentrations decrease. A second nucleation mode maximum follows in summer, likely attributable to vegetation related biogenic sources.

Cluster analysis, as described in Sects. 2.3.5 and 3.2, was also performed to separate the non-normalized size and mass distributions. As a result of this clustering, most of the data appears to fall into a category of bi-modal number size distributions, with maxima in Aitken and accumulation modes at sizes 50 and 200 nm, respectively (Fig. 5a, clusters: 1, 2). Cluster 1 is the most common cluster type observed, it has both continental and marine influences, and the lowest average number concentration ($212 \pm 127\,cm^{-3}$) of all the clusters. Cluster 2, which is the second most common type, is clearly more continental, which results in an increase of the particle number in both the observed particle modes. The third most common cluster is number 7, which based on the corresponding meteorological variables (high temperature, relatively low RH and high radiation) and the air mass source analysis (Table 4), best represents mid-summer continental air flow. An increase of an Aitken mode aerosols in cluster 2 indicates the proximity of local sources in addition to long-range transport represented by the accumulation mode.

The most striking feature in Fig. 5a (and Table 4) is the separation of the marine and continental air with respect to their accumulation mode concentrations. The four most continental clusters (numbers 2, 5, 6, 7) present higher and similar, accumulation mode concentrations in comparison to the four most marine cluster types. Where these clusters differ is in Aitken and nucleation mode concentrations. Cluster 5 characterizes the calmest winter days with continental air with strong inversions and the consequent of accumulation of pollutants in the Aitken mode. Clusters 6 and 7 are mostly continental,

ACPD
15, 18109–18149, 2015

and represent conditions with higher temperatures and wind speeds resulting in more efficient mixing and dilution of air in comparison to cluster 5.

Another prominent feature characterizing the clusters 3, 4 and 8 is large radiation values and the highest nucleation mode concentrations. It appears that nucleation is more common in marine as opposed to continental, air masses; this phenomena has been documented in previous studies (Sogacheva et al., 2008; Asmi et al., 2011). Cluster 8 to 4 and 3 (in this order) show decreasing nucleation mode concentrations corresponding to increasing continental influence, RH and temperature and decreasing radiation. Increasing RH and decreasing radiation could be linked with cloudiness inhibiting nucleation (Sogacheva et al., 2008; Hamed et al., 2011). Interestingly, nucleation seemed also less likely with increasing wind speeds which might be explained by more efficient dilution of nucleating and condensing vapors or scavenging of nucleating clusters. This further implies that nucleation at Tiksi is connected to sources near the surface, most likely to biogenic VOC emissions, which requires confirmation by additional analysis.

Mass distribution clusters present a different picture in terms of differentiating air mass characteristics. The most prevalent clusters in decreasing order are numbers 5, 6 and 7 (Fig. 5b). Of these, only cluster 5 seems to be representative of a marine air mass with less than 50 % continental influences. In addition, cluster 5 has the lowest mass concentrations of all the clusters (but also a high variance of concentrations) and is characterized with the highest humidity, relatively high average radiation and average temperatures just above zero. The mass size distribution measured by APS for cluster 5 differs from that of the other clusters, showing only one major mode at around 2 µm size. Interestingly, of all the clusters, this cluster 5 has the highest mass at nucleation mode sizes. In fact, the inverse correlation of nucleation and accumulation or coarse mode concentrations is pronounced in all the mass size distribution clusters observed. Compared to cluster 5, clusters 6 and 7 are clearly more continental leading to an increased total mass concentration to a corresponding decreased nucleation mode mass.

ACPD
15, 18109–18149, 2015

Clusters 4, 3 and 8 all showed elevated mass concentrations, with averages of 65.1, 44.7 and 20.4 $\mu g\,m^{-3}$ (from DMPS only) respectively. They are characterized by strong continental influences, and high average temperatures, indicating that they occur in summer continental air flows. Clusters 3 and 4 occurred only on 9 and 11 July 2012 and represent long-range transport of biomass burning aerosols from southern the Yakutian region, as indicated by MODIS active fire records combined with back-trajectory calculations. Furthermore, in-situ aerosol absorption measurements indicated elevated black carbon (BC) concentrations on both of these days. The uncorrected aethalometer data (at: http://www.esrl.noaa.gov/psd/iasoa/) show black carbon concentrations up to 2 $\mu g\,m^{-3}$. Another set of related days inside of cluster 8 are: 26 July, 01–02 August 2012, 25 September 2012, and 12–13 August 2013. For these days the back-trajectory calculations also indicate transport from southerly directions, where MODIS recorded forest fire activity; simultaneously, the measured BC concentration at Tiksi was elevated to around 1 $\mu g\,m^{-3}$).

Cluster 2 shows an average mass concentration of 9.8 $\mu g\,m^{-3}$, which is less than the concentrations characterizing the biomass burning event cases, yet higher than concentrations typical to Tiksi. Average temperature for cluster 2 is high (14.2 °C), values of global radiation are the highest and RH is the lowest of all the clusters. It seems therefore likely that this cluster represents summer continental air masses that are strongly affected by biogenic sources and secondary particle formation. Since the process of secondary particle formation from biogenic precursors is dependent on light providing the atmospheric oxidizing capacity, the conditions of high radiation and low RH (indicating low cloudiness) are favorable for this process (Hamed et al., 2011). It is therefore concluded that as a result of secondary particle formation taking place in summer over Siberian forested areas, the aged accumulation mode aerosols are grown by the condensing vapors from the oxidized biogenic volatile organic compounds (VOC) that are observed in Tiksi, and further grouped in cluster 2. Verification of this hypothesis will require a more detailed source region analysis with additional measurements of particle chemical composition.

ACPD
15, 18109–18149, 2015

Cluster 1 falls between clusters 2 and 7 in prevalence, as well as other characteristic quantities: mass concentrations, temperature, RH and radiation. It was therefore assumed to contain mixed cases of both, not clearly belonging to either one of the other two cluster types.

3.4 Seasonal influences on aerosol properties

3.4.1 Continental biogenic sources driving the cloud condensation nuclei concentrations in summer

Similar to previous observations in the boreal forest zone (Tunved et al., 2006; Asmi et al., 2011; Väänänen et al., 2013), observations at Tiksi indicate increasing submicron aerosol particle mass with increasing time over continent (Fig. 6). The increase is larger by an order of magnitude when temperatures exceeds 0 °C, although at temperatures < 0 °C some increase in aerosol mass can be still be observed with longer time over continent (Fig. 6b). This is expected considering the strong temperature dependency of biogenic VOC emissions (e.g., Guenther et al., 2006).

Tunved et al. (2006) showed that the aerosol mass load over the Finnish Arctic site Pallas depends on the air mass time over the continent and follows a linear fit $y = 0.014x + 0.12$, where y represents the aerosol mass and x the time spent over the continent and April–September DMPS data for sizes < 450 nm were used for fitting. Fitting for the Tiksi data was also done using only summertime data and particle sizes < 500 nm; the resulting fit $y = 0.018x - 0.05$ (Fig. 7a), indicates a similar or even higher, mass increase over the Siberian continental region in comparison to Nordic boreal forest. Additionally, Tiksi data suggests a quadratic than linear dependence, which might be a secondary effect of the observed temperature dependence of the continental air masses. The most continental air masses also possessed the warmest temperatures, therefore it is likely that they originating further from the south, with denser vegetation as well as higher VOC emission rates (Guenther et al., 2006).

ACPD
15, 18109–18149, 2015

As a direct consequence of secondary aerosol formation, the number of the largest particles that are capable of acting as cloud condensation nuclei (CCN), tends to increase. This has been shown for several sites that were characterized by relatively clean and cold environments and affected by biogenic VOCs by Paasonen et al. (2013). They also linked the CCN concentrations with measured monoterpenes. In their study Paasonen et al. (2013) used aerosol number concentration over the limit of 100 nm as a proxy for the CCN, which will be here referred to as CCN_{100}.

In Tiksi, the CCN_{100} concentration also increased as a function of temperature (Fig. 7b). While the average CCN_{100} concentration remained below 200 cm^{-3} throughout most of the year, at > 10 °C an exponential increase as a function of temperature was observed. Paasonen et al. (2013) also showed an increase of CCN_{100} as a function of temperature with exponential fits for two Finnish, one Canadian and one Russian Siberian sites. When CCN_{100} was fitted as a function of temperature (T)

$$CCN_{100} = \alpha \exp(\beta T) \quad (2)$$

they obtained β values varying between 0.029 and 0.085. Data from Tiksi plotted for a similar temperature range > 5 °C, shows even a higher temperature dependence with β value of 0.126 (Fig. 7b). This confirms a major biological contribution to Tiksi aerosol populations during summer and suggests a strong temperature feedback for aerosols in Arctic Siberia. Possible reasons for the deviating temperature dependencies observed for the five different sites include differences in the relative importance of other (anthropogenic) sources as well as the different vegetation types. In comparison to European boreal forest emissions, which are largely dominated by α-pinene (Rinne et al., 2000; Tarvainen et al., 2005), Siberian larches emit mainly sabinene (Ruuskanen et al., 2007) leading to different oxidation chemistry and consequently different aerosol yields (e.g., Griffin et al., 1999). In addition to natural vegetation sources, another temperature dependent aerosol source in summer Siberia are the intense fire events, as already discussed in Sect. 3.3.

ACPD
15, 18109–18149, 2015

In context of the entire Tiksi annual temperature range, the maximum average CCN_{100} concentration of 1130 cm^{-3} was observed at temperatures > 30 °C (Fig. 8a). However, these extreme hot days are rare in Tiksi and only 13 cases were available for calculations. The average CCN_{100} concentrations were lower in marine in comparison to continental air masses. The increase of CCN_{100} with temperature was only observed in continental air masses, providing further evidence of the importance of continental biogenic VOC or fire related sources. However, the comparison of continental and marine air masses is somewhat obscured by the lack of warm Arctic marine air.

The CCN_{100} concentrations can be compared with the total aerosol number concentrations to indicate changes in aerosol number size distributions. Ratio of these numbers stayed around 0.5 during most of the year in both of the air mass types (Fig. 8b). However, during summer (at temperatures above zero), this ratio decreased to close to 0.1 in marine air masses, thus indicating an increasing total number concentration caused by the smallest particles. In continental air masses the CCN_{100} to number ratio showed an incremental decrease as a function of temperature in the range of 0–15 °C, which was followed by a strong increase of CCN_{100} with temperature. In a global perspective this result can be compared with those of Andreae (2009) indicating that the CCN and particle number concentrations and their ratios in Tiksi during marine and continental air flows are representative of remote marine and remote continental sites.

3.4.2 Accumulation of pollutants on calm and cold days

There are many indications in the Tiksi data of a severe pollution occurring during cold and calm weather. This was studied in detail when wind speeds decreased to values close to 1 $m\,s^{-1}$ (a threshold for data quality checks) resulting in increasing number concentrations (Fig. 9). This was particularly true for Aitken mode particles, indicating an influence from local or regional pollution sources, but CCN_{100} concentrations in accumulation mode were also elevated during the coldest episodes. As these are likely caused by strong cold-weather inversions, and contain episodes lasting for hours or even days, it is not clear if these should be considered as local air pollution events

ACPD
15, 18109–18149, 2015

and removed from the analysis, or rather as more regional pollution occurring over vast areas in northern Siberia. At wind speeds $> 2\,m\,s^{-1}$ such pollution episodes become rare and therefore, in order to exclude them this limit can be used. However, calm days are common during winter months and their exclusion also removes a large fraction of wintertime data.

4 Conclusions

Aerosols measured in Tiksi show a large interannual variability in terms of particle size, number and mass distributions. The monthly median total aerosol number concentration in Tiksi ranges from $184\,cm^{-3}$ in November to $724\,cm^{-3}$ in July with a local maximum in March of $481\,cm^{-3}$. The total mass concentration has a distinct maximum in February–March of $1.72–2.38\,\mu g\,m^{-3}$ and two minimums in June of $0.42\,\mu g\,m^{-3}$ and in September–October of $0.36–0.57\,\mu g\,m^{-3}$.

The influence of the vast, vegetated Siberian regions on aerosol characteristics is the most evident in summer when the number concentration reaches a maximum. Results indicate this is related to secondary particle formation and growth by biogenic organic compounds, and to some extent also on biomass burning. Both of these sources increase particle number, but also the mass and the concentrations of cloud condensation nuclei (CCN), thereby being important modulators of the summertime Arctic climate. Increase of CCN and particle mass are only seen in continental air masses, and have a strong correlation with temperature.

In winter and spring, the size distributions are dominated by larger accumulation and coarse mode particles influenced by Arctic haze. Elevated mass concentrations are measured until April after which another maximum in mass occurs in July–August. The second mass maximum is lower in amplitude and mainly results from increased accumulation mode aerosol mass distributions rather than coarse mode aerosol mass distributions. Additionally, during calm and cold winter periods, severe pollution episodes

ACPD
15, 18109–18149, 2015

can occur due to local inversions leading to an accumulation of particles close to the surface.

The relative impact of local and regional Arctic sources in comparison to long-range transportation on the process of new particle formation has not yet been examined. Nucleation mode particles are frequently observed in Tiksi during early spring and summer and the formation of these particles is favored in marine air masses. This suggests either a marine source of nucleating vapors or a lower background concentration and thereby a decreased sink for particles and vapors at a coastal zone.

The results presented here highlight some of the important climate feedbacks related with Arctic aerosols and sets the stage for quantitative future studies on source identification.

The Supplement related to this article is available online at doi:10.5194/acpd-15-18109-2015-supplement.

Acknowledgements. This work was supported by the Academy of Finland project Greenhouse gas, aerosol and albedo variations in the changing Arctic (project number 269095) and the Academy of Finland Center of Excellence program (project number 272041), KONE foundation (grant number 46-6817) and Magnus Ehrnooth foundation grant for "Natural climate feedbacks of aerosols in the Arctic". Data collection, acquisition, transfer and archiving was supported by the Roshydromet Arctic and Antarctic Research institute and the NOAA Earth Systems Research Laboratory Physical Science Division. We also like to thank E. D. Volkov and O. V. Dmitrieva for maintaining the measurements in Tiksi year-round.

References

Andreae, M. O.: Correlation between cloud condensation nuclei concentration and aerosol optical thickness in remote and polluted regions, Atmos. Chem. Phys., 9, 543–556, doi:10.5194/acp-9-543-2009, 2009. 18128

Asmi, E., Kivekäs, N., Kerminen, V.-M., Komppula, M., Hyvärinen, A.-P., Hatakka, J., Viisanen, Y., and Lihavainen, H.: Secondary new particle formation in Northern Finland Pallas site between the years 2000 and 2010, Atmos. Chem. Phys., 11, 12959–12972, doi:10.5194/acp-11-12959-2011, 2011. 18111, 18123, 18124, 18126

Asmi, E., Freney, E., Hervo, M., Picard, D., Rose, C., Colomb, A., and Sellegri, K.: Aerosol cloud activation in summer and winter at puy-de-Dôme high altitude site in France, Atmos. Chem. Phys., 12, 11589–11607, doi:10.5194/acp-12-11589-2012, 2012. 18111

Beddows, D. C. S., Dall'Osto, M., and Harrison, R. M.: Cluster analysis of rural, urban, and curbside atmospheric particle size data, Environ. Sci. Technol., 43, 4694–4700, doi:10.1021/es803121t, 2009. 18118

Bodhaine, B. A.: Barrow surface aerosol – 1976–1986, Atmos. Environ., 23, 2357–2369, doi:10.1016/0004-6981(89)90249-7, 1989. 18111, 18122

Bond, T. C., Doherty, S. J., Fahey, D. W., Forster, P. M., Berntsen, T., DeAngelo, B. J., Flanner, M. G., Ghan, S., Kärcher, B., Koch, D., Kinne, S., Kondo, Y., Quinn, P. K., Sarofim, M. C., Schultz, M. G., Schulz, M., Venkataraman, C., Zhang, H., Zhang, S., Bellouin, N., Guttikunda, S. K., Hopke, P. K., Jacobson, M. Z., Kaiser, J. W., Klimont, Z., Lohmann, U., Schwarz, J. P., Shindell, D., Storelvmo, T., Warren, S. G., and Zenderm, C. S.: Bounding the role of black carbon in the climate system: a scientific assessment, J. Geophys. Res.-Atmos., 118, 5380–5552, doi:10.1002/jgrd.50171, 2013. 18110, 18111

Bourgeois, Q. and Bey, I.: Pollution transport efficiency toward the Arctic: sensitivity to aerosol scavenging and source regions, J. Geophys. Res., 116, D08213, doi:10.1029/2010JD015096, 2011. 18111

Chi, X., Winderlich, J., Mayer, J.-C., Panov, A. V., Heimann, M., Birmili, W., Heintzenberg, J., Cheng, Y., and Andreae, M. O.: Long-term measurements of aerosol and carbon monoxide at the ZOTTO tall tower to characterize polluted and pristine air in the Siberian taiga, Atmos. Chem. Phys., 13, 12271–12298, doi:10.5194/acp-13-12271-2013, 2013. 18111

Draxler, R. R.: HYSPLIT4 user's guide, NOAA Tech. Memo. ERL ARL-230, NOAA Air Resources Laboratory, Silver Spring, MD, USA, 1999. 18118

Draxler, R. R. and Hess, G. D.: Description of the HYSPLIT_4 modeling system, NOAA Tech. Memo. ERL ARL-224, NOAA Air Resources Laboratory, Silver Spring, MD, USA, 24 pp., 1997. 18118

Draxler, R. R. and Hess, G. D.: An overview of the HYSPLIT_4 modeling system of trajectories, dispersion, and deposition, Aust. Meteorol. Mag., 47, 295–308, 1998. 18118

ACPD
15, 18109–18149, 2015

Griffin, R. T., Cocker III, D. R., Flagan, R. C., and Seinfeld, J. H.: Organic aerosol formation from the oxidation of biogenic hydrocarbons, J. Geophys. Res., 104, 3555–3567, 1999. 18127

Guenther, A., Karl, T., Harley, P., Wiedinmyer, C., Palmer, P. I., and Geron, C.: Estimates of global terrestrial isoprene emissions using MEGAN (Model of Emissions of Gases and Aerosols from Nature), Atmos. Chem. Phys., 6, 3181–3210, doi:10.5194/acp-6-3181-2006, 2006. 18126

Hamed, A., Korhonen, H., Sihto, S.-L., Joutsensaari, J., Järvinen, H., Petäjä, T., Arnold, F., Nieminen, T., Kulmala, M., Smith, J. N., Lehtinen, K. E. J., and Laaksonen, A.: The role of relative humidity in continental new particle formation, J. Geophys. Res., 116, D03202, doi:10.1029/2010JD014186, 2011. 18124, 18125

Heintzenberg, J., Birmili, W., Theiss, D., and Kisilyakhov, Y.: The atmospheric aerosol over Siberia, as seen from the 300 m ZOTTO tower, Tellus B, 60, 276–285, 2008. 18111

Heintzenberg, J., Birmili, W., Otto, R., Andreae, M. O., Mayer, J.-C., Chi, X., and Panov, A.: Aerosol particle number size distributions and particulate light absorption at the ZOTTO tall tower (Siberia), 2006–2009, Atmos. Chem. Phys., 11, 8703–8719, doi:10.5194/acp-11-8703-2011, 2011. 18111

Hienola, A. I., Pietikäinen, J.-P., Jacob, D., Pozdun, R., Petäjä, T., Hyvärinen, A.-P., Sogacheva, L., Kerminen, V.-M., Kulmala, M., and Laaksonen, A.: Black carbon concentration and deposition estimations in Finland by the regional aerosol–climate model REMO-HAM, Atmos. Chem. Phys., 13, 4033–4055, doi:10.5194/acp-13-4033-2013, 2013. 18111

Laakso, L., Hussein, T., Aarnio, P., Komppula, M., Hiltunen, V., Viisanen, Y., and Kulmala, M.: Diurnal and annual characteristics of particle mass and number concentrations in urban, rural and Arctic environments in Finland, Atmos. Environ., 37, 2629–2641, 2003. 18122

Liu, X., Easter, R. C., Ghan, S. J., Zaveri, R., Rasch, P., Shi, X., Lamarque, J.-F., Gettelman, A., Morrison, H., Vitt, F., Conley, A., Park, S., Neale, R., Hannay, C., Ekman, A. M. L., Hess, P., Mahowald, N., Collins, W., Iacono, M. J., Bretherton, C. S., Flanner, M. G., and Mitchell, D.: Toward a minimal representation of aerosols in climate models: description and evaluation in the Community Atmosphere Model CAM5, Geosci. Model Dev., 5, 709–739, doi:10.5194/gmd-5-709-2012, 2012. 18111

Mauritsen, T., Sedlar, J., Tjernström, M., Leck, C., Martin, M., Shupe, M., Sjogren, S., Sierau, B., Persson, P. O. G., Brooks, I. M., and Swietlicki, E.: An Arctic CCN-limited cloud-aerosol regime, Atmos. Chem. Phys., 11, 165–173, doi:10.5194/acp-11-165-2011, 2011. 18111

ACPD
15, 18109–18149, 2015

Mitchell, J. M.: Visual range in the polar regions with particular reference to the Alaskan Arctic, J. Atmos. Terr. Phys., 17, 195–211, 1957. 18111

Paasonen, P., Asmi, A., Petäjä, T., Kajos, M. K., Äijälä, M., Junninen, H., Holst, T., Abbatt, J. P. D., Arneth, A., Birmili, W., van der Gon, H. D., Hamed, A., Hoffer, A., Laakso, L., Laaksonen, A., Leaitch, W. R., Plass-Dülmer, C. Pryor, S. C., Räisänen, P., Swietlicki, E., Wiedensohler, A., Worsnop, D. R., Kerminen, V.-M., and Kulmala, M.: Warming-induced increase in aerosol number concentration likely to moderate climate change, Nat. Geosci., 6, 438–442, doi:10.1038/ngeo1800, 2013. 18111, 18127

Quinn, P. K., Miller, T. L., Bates, T. S., Ogren, J. A., Andrews, E., and Shaw, G. E.: A 3-year record of simultaneously measured aerosol chemical and optical properties at Barrow, Alaska, J. Geophys. Res.-Atmos., 107, 4130, doi:10.1029/2001JD001248, 2002. 18122

Richter-Menge, J., Overland, J., Proshutinsky, A., Romanovsky, V., Bengtsson, L., Brigham, L., Dyurgerov, M., Gascard, J. C., Gerland, S., Graversen, R., Haas, C., Karcher, M., Kuhry, P., Maslanik, J., Melling, H., Maslowski, W., Morison, J., Perovich, D., Przybylak, R., Rachold, V., Rigor, I., Shiklomanov, A., Stroeve, J., Walker, D., and Walsh, J.: State of the Arctic Report, NOAA OAR Special Report, NOAA/OAR/PMEL, Seattle, WA, USA, 36 pp., 2006. 18110

Rinne, J., Hakola, H., Laurila, T., and Rannik, U.: Canopy scale monoterpene emissions of pinus sylvestris dominated forests, Atmos. Environ., 34, 1099–1107, doi:10.1016/S1352-2310(99)00335-0, 2000. 18127

Ruuskanen, T. M., Kajos, M., Hellén, H., Hakola, H., Tarvainen, V., and Rinne, J.: Volatile organic compound emissions from Siberian larch, Atmos. Environ., 41, 5807–5812, 2007. 18127

Saarikoski, S., Mäkelä, T., Hillamo, R., Aalto, P. P., Kerminen, V.-M., and Kulmala, M.: Physico-chemical characterization and mass closure of size-segregated atmospheric aerosols in Hyytiälä, Finland, Boreal Environ. Res., 10, 385–400, 2005. 18117

Shindell, D. and Faluvegi, G.: Climate response to regional radiative forcing during the twentieth century, Nat. Geosci., 2, 294–300, 2009. 18110

Sogacheva, L., Saukkonen, L., Nilsson, E. D., Dal Maso, M., Schultz, D. M., De Leeuw, G., and Kulmala, M.: New aerosol particle formation in different synoptic situations at Hyytiälä Southern Finland, Tellus B, 60, 485–494, 2008. 18124

Stock, M., Ritter, C., Aaltonen, V., Aas, W., Handorff, D., Herber, A., Treffeisen, R., and Dethloff, K.: Where does the optically detectable aerosol in the European Arctic come from?, Tellus B, 66, 21450, doi:10.3402/tellusb.v66.21450, 2014. 18111

ACPD
15, 18109–18149, 2015

Stohl, A., Klimont, Z., Eckhardt, S., Kupiainen, K., Shevchenko, V. P., Kopeikin, V. M., and Novigatsky, A. N.: Black carbon in the Arctic: the underestimated role of gas flaring and residential combustion emissions, Atmos. Chem. Phys., 13, 8833–8855, doi:10.5194/acp-13-8833-2013, 2013. 18111

Stolzenburg, M.: An Ultrafine Aerosol Size Distribution Measuring System, PhD thesis, Mechanical Engineering Department, University of Minnesota, USA, 1988. 18115

Tarvainen, V., Hakola, H., Hellén, H., Bäck, J., Hari, P., and Kulmala, M.: Temperature and light dependence of the VOC emissions of Scots pine, Atmos. Chem. Phys., 5, 989–998, doi:10.5194/acp-5-989-2005, 2005. 18127

Tunved, P., Hansson, H.-C., Kulmala, M., Aalto, P., Viisanen, Y., Karlsson, H., Kristensson, A., Swietlicki, E., Dal Maso, M., Ström, J., and Komppula, M.: One year boundary layer aerosol size distribution data from five nordic background stations, Atmos. Chem. Phys., 3, 2183–2205, doi:10.5194/acp-3-2183-2003, 2003. 18122

Tunved, P., Hansson, H.-C., Kerminen, V.-M., Ström, J., Dal Maso, M., Lihavainen, H., Viisanen, Y., Aalto, P. P., Komppula, M., and Kulmala, M.: High natural aerosol loading over boreal forests, Science, 312, 261–263, 2006. 18111, 18126

Tunved, P., Ström, J., and Krejci, R.: Arctic aerosol life cycle: linking aerosol size distributions observed between 2000 and 2010 with air mass transport and precipitation at Zeppelin station, Ny-Ålesund, Svalbard, Atmos. Chem. Phys., 13, 3643–3660, doi:10.5194/acp-13-3643-2013, 2013. 18111, 18122

United States Geological Survey: Global Multi-resolution Terrain Elevation Data 2010, available at http://earthexplorer.usgs.gov/ (last access: 06 May 2015), 2015. 18141

Uttal, T., Makshtas, A., and Laurila, T.: The Tiksi International Hydrometeorological Observatory – An Arctic Members Partnership, WMO Bulletin, 62, 22–26, 2013. 18112, 18113

Väänänen, R., Kyrö, E.-M., Nieminen, T., Kivekäs, N., Junninen, H., Virkkula, A., Dal Maso, M., Lihavainen, H., Viisanen, Y., Svenningsson, B., Holst, T., Arneth, A., Aalto, P. P., Kulmala, M., and Kerminen, V.-M.: Analysis of particle size distribution changes between three measurement sites in northern Scandinavia, Atmos. Chem. Phys., 13, 11887–11903, doi:10.5194/acp-13-11887-2013, 2013. 18126

Viskari, T., Asmi, E., Virkkula, A., Kolmonen, P., Petäjä, T., and Järvinen, H.: Estimation of aerosol particle number distribution with Kalman Filtering – Part 2: Simultaneous use of DMPS, APS and nephelometer measurements, Atmos. Chem. Phys., 12, 11781–11793, doi:10.5194/acp-12-11781-2012, 2012. 18117

ACPD
15, 18109–18149, 2015

Walsh, J. E. and Chapman, W. L.: Arctic cloud–radiation–temperature associations in observational data and atmospheric reanalysis, J. Climate, 11, 3030–3045, 1998. 18111

Wiedensohler, A.: Die bipolare Diffusionsaufladung von Partikeln in chemisch trägen Reinstgasen, PhD thesis, University of Duisburg, Germany, 1989. 18115

Wiedensohler, A., Birmili, W., Nowak, A., Sonntag, A., Weinhold, K., Merkel, M., Wehner, B., Tuch, T., Pfeifer, S., Fiebig, M., Fjäraa, A. M., Asmi, E., Sellegri, K., Depuy, R., Venzac, H., Villani, P., Laj, P., Aalto, P., Ogren, J. A., Swietlicki, E., Williams, P., Roldin, P., Quincey, P., Hüglin, C., Fierz-Schmidhauser, R., Gysel, M., Weingartner, E., Riccobono, F., Santos, S., Grüning, C., Faloon, K., Beddows, D., Harrison, R., Monahan, C., Jennings, S. G., O'Dowd, C. D., Marinoni, A., Horn, H.-G., Keck, L., Jiang, J., Scheckman, J., McMurry, P. H., Deng, Z., Zhao, C. S., Moerman, M., Henzing, B., de Leeuw, G., Löschau, G., and Bastian, S.: Mobility particle size spectrometers: harmonization of technical standards and data structure to facilitate high quality long-term observations of atmospheric particle number size distributions, Atmos. Meas. Tech., 5, 657–685, doi:10.5194/amt-5-657-2012, 2012. 18114, 18115

ACPD
15, 18109–18149, 2015

Table 1. Total particle number concentration (N), temperature (T), RH, solar radiation (Rad), wind speed (Ws) and percentage over continental areas (Cont), for different normalized number size distribution clusters (numbers 1–8, referring to Fig. 3a). Number of cases available for each cluster is shown in parenthesis below the cluster number. For different variables both average (upper row) and median (lower row) are calculated, and for total number also standard deviation is presented.

Cluster no. (cases)	N [cm^{-3}]	T [°C]	RH [%]	Rad [W m^{-2}]	Ws [m s^{-1}]	Cont [%]
1	1365 ± 1064	0.2	70	153	3.1	81
(691)	1138	8.6	72	65	2.4	95
2	1204 ± 1275	–3.2	76	139	3.2	71
(1289)	820	4.1	77	49	2.5	74
3	766 ± 950	1.1	82	138	4.2	53
(1104)	501	3.2	84	67	3.7	49
4	435 ± 620	–2.7	81	111	4.4	60
(1286)	257	1.3	83	35	3.9	62
5	561 ± 1090	–9.1	78	148	4.5	53
(444)	266	–6.6	79	18	3.9	44
6	745 ± 1265	–1.0	81	141	4.4	47
(1361)	366	1.3	82	52	3.7	40
7	395 ± 337	–8.0	77	99	5.1	77
(2481)	291	–7.3	77	11	4.3	99
8	299 ± 342	–7.8	79	111	5.5	64
(3979)	192	–6.6	80	19	4.8	70

ACPD
15, 18109–18149, 2015

Table 2. Total particle mass concentration from DMPS data (M), from APS data (M_{APS}), temperature (T), RH, solar radiation (Rad), wind speed (Ws) and percentage over continental areas (Cont), for different normalized mass size distribution clusters (numbers 1–8, referring to Fig. 3b). Number of cases available for each cluster is shown in parenthesis below the cluster number, and the number of cases from APS after this. For different variables both average (upper row) and median (lower row) are calculated, and for total number also standard deviation is presented.

Cluster no. (cases/APS)	M [$\mu g\,m^{-3}$]	M_{APS} [$\mu g\,m^{-3}$]	T [°C]	RH [%]	Rad [$W\,m^{-2}$]	Ws [$m\,s^{-1}$]	Cont [%]
1	2.1 ± 2.1	1.3 ± 1.6	–9.4	78	112	5.1	76
(1595/541)	1.5	1.0	–10.4	78	17	4.4	94
2	2.2 ± 4.1	2.0 ± 2.2	–17.2	74	71	4.3	66
(2529/638)	1.4	1.4	–23.9	73	0	3.4	74
3	1.5 ± 1.2	0.6 ± 0.7	0.8	70	188	2.7	71
(328/139)	1.1	0.3	9.3	70	63	2.0	77
4	1.1 ± 1.5	0.8 ± 1.4	0.9	80	126	4.8	64
(2700/945)	0.6	0.4	1.7	82	48	4.2	68
5	0.4 ± 0.5	0.3 ± 0.6	3.4	84	123	4.2	53
(638/145)	0.3	0.2	3.8	86	57	3.9	45
6	0.4 ± 0.5	0.4 ± 0.6	6.3	79	184	4.3	41
(1484/596)	0.3	0.2	6.2	83	119	3.9	35
7	0.8 ± 0.9	3.8 ± 4.3	–9.3	82	76	5.9	34
(510/135)	0.4	2.2	–4.4	83	1	5.1	24
8	1.6 ± 1.4	1.0 ± 1.1	–4.3	79	134	4.9	77
(2851/1156)	1.2	0.7	–5.0	81	37	4.2	90

ACPD
15, 18109–18149, 2015

Table 3. Average and median number and mass concentrations for different months. First column indicate the month and second column (N) the amount of data used in averaging for DMPS and APS instruments. The following columns present monthly average ($\overline{N}_{TO}$, $\overline{N}_{NU}$, $\overline{N}_{AI}$, $\overline{N}_{AC}$, $\overline{N}_{CO}$, $\overline{M}_{TO}$, $\overline{M}_{CO}$) and median ($\tilde{N}_{TO}$, $\tilde{N}_{NU}$, $\tilde{N}_{AI}$, $\tilde{N}_{AC}$, $\tilde{N}_{CO}$, $\tilde{M}_{TO}$, $\tilde{M}_{CO}$) values calculated for total (7–500 nm), nucleation mode (7–25 nm), Aitken mode (25–100 nm), accumulation mode (100–500 nm) and coarse mode (> 410 nm) number and for DMPS and APS total mass, respectively.

Month	N (DMPS/APS) [cases]	$\overline{N}_{TO}$ ($\tilde{N}_{TO}$) [cm^{-3}]	$\overline{N}_{NU}$ ($\tilde{N}_{NU}$) [cm^{-3}]	$\overline{N}_{AI}$ ($\tilde{N}_{AI}$) [cm^{-3}]	$\overline{N}_{AC}$ ($\tilde{N}_{AC}$) [cm^{-3}]	$\overline{N}_{CO}$ ($\tilde{N}_{CO}$) [cm^{-3}]	$\overline{M}_{TO}$ ($\tilde{M}_{TO}$) [µg m^{-3}]	$\overline{M}_{CO}$ ($\tilde{M}_{CO}$) [µg m^{-3}]
1	4534/1734	469 (200)	36 (10)	297 (69)	139 (112)	5.3 (5.0)	1.38 (1.24)	1.60 (1.07)
2	4070/1680	639 (329)	83 (27)	370 (119)	222 (182)	7.4 (6.3)	2.03 (1.72)	1.72 (1.64)
3	4825/2472	762 (481)	146 (19)	358 (140)	276 (267)	5.0 (4.8)	2.60 (2.38)	1.69 (1.36)
4	7470/7512	725 (396)	130 (14)	341 (123)	258 (222)	4.3 (4.0)	2.18 (1.89)	1.74 (1.31)
5	9903/6028	529 (222)	89 (12)	259 (69)	185 (113)	3.5 (1.8)	1.59 (0.96)	1.18 (0.70)
6	7776/4656	620 (327)	142 (26)	338 (147)	144 (71)	1.2 (0.7)	0.95 (0.42)	0.34 (0.24)
7	10701/9267	970 (724)	172 (35)	567 (343)	241 (102)	1.0 (0.4)	1.94 (0.60)	1.01 (0.32)
8	11570/9572	590 (383)	111 (19)	322 (161)	160 (90)	4.3 (1.1)	1.41 (0.56)	1.15(0.48)
9	12651/6606	324 (222)	61 (18)	160 (98)	105 (60)	1.0 (0.7)	0.83 (0.36)	0.74 (0.46)
10	11950/7627	302 (227)	64 (21)	150 (98)	90 (76)	1.5 (1.1)	0.70 (0.57)	1.39 (0.45)
11	8534/9910	280 (184)	38 (15)	143 (68)	106 (98)	4.0 (3.1)	1.04 (0.94)	1.70 (0.83)
12	2891/0	415 (253)	71 (23)	220 (84)	126 (116)	–	1.35 (1.33)	–

ACPD
15, 18109–18149, 2015

Table 4. Total particle number concentration (N), temperature (T), RH, solar radiation (Rad), wind speed (Ws) and percentage over continental areas (Cont), for different size distribution clusters (numbers 1–8, referring to Fig. 5a). Number of cases available for each cluster is shown in parenthesis below the cluster number. For different variables both average (upper row) and median (lower row) are calculated, and for total number also standard deviation is presented.

Cluster no. (cases)	N [cm^{-3}]	T [°C]	RH [%]	Rad [$W m^{-2}$]	Ws [$m s^{-1}$]	Cont [%]
1	212 ± 127	–7.5	81	97	5.0	57
(7991)	190	–4.6	82	15	4.4	56
2	706 ± 322	–0.3	76	139	4.6	81
(2954)	641	3.3	78	59	3.8	99
3	1648 ± 811	2.7	77	217	3.9	52
(491)	1498	5.7	79	144	3.3	47
4	4300 ± 1264	–6.7	71	360	2.4	51
(83)	3951	–6.4	70	390	1.8	38
5	8844 ± 2327	–29.6	65	89	1.1	88
(17)	7846	–42.4	59	10	1.1	100
6	3274 ± 1205	–11.8	68	156	2.3	73
(252)	2903	–14.3	67	26	1.5	78
7	1572 ± 527	0.3	67	182	3.0	79
(839)	1464	11.2	68	92	2.2	87
8	11 054 ± 4194	–12.0	66	508	1.7	45
(8)	10 486	–20.3	73	484	1.7	26

ACPD
15, 18109–18149, 2015

Table 5. Total particle mass concentration from DMPS data (M), from APS data (M_{APS}), temperature (T), RH, solar radiation (Rad), wind speed (Ws) and percentage over continental areas (Cont), for different size distribution clusters (numbers 1–8, referring to Fig. 5b). Number of cases available for each cluster is shown in parenthesis below the cluster number, and the number of cases from APS after this. For different variables both average (upper row) and median (lower row) are calculated, and for total number also standard deviation is presented.

Cluster no. (cases/APS)	M [$\mu g\,m^{-3}$]	M_{APS} [$\mu g\,m^{-3}$]	T [°C]	RH [%]	Rad [$W\,m^{-2}$]	Ws [$m\,s^{-1}$]	Cont [%]
1	6.0 ± 0.8	1.9 ± 1.5	7.1	71	172	5.0	93
(319/118)	5.8	1.4	8.4	73	94	4.5	100
2	9.8 ± 1.8	2.5 ± 1.3	14.2	59	253	5.0	91
(96/39)	9.3	2.3	18.9	57	226	4.6	100
3	44.7 ± 3.8	–	16.4	82	16	4.9	94
(7/–)	45.7	–	16.1	84	14	5.1	100
4	65.1 ± 4.9	–	18.2	79	10	3.8	98
(4/–)	64.2	–	18.8	82	6	3.8	98
5	0.4 ± 0.2	0.5 ± 0.9	1.2	83	133	4.4	47
(5268/1737)	0.3	0.2	2.4	85	57	4.0	40
6	1.3 ± 0.4	1.4 ± 2.0	–13.2	76	88	4.9	70
(4831/1689)	1.2	0.9	–13.1	76	1	4.0	80
7	3.0 ± 0.9	1.5 ± 1.7	–4.5	74	151	4.7	88
(2078/698)	2.8	1.1	–3.3	76	65	3.7	100
8	20.4 ± 2.6	8.0 ± 0.7	13.6	79	108	3.0	94
(32/16)	20.0	7.9	14.9	85	61	2.4	100

ACPD
15, 18109–18149, 2015

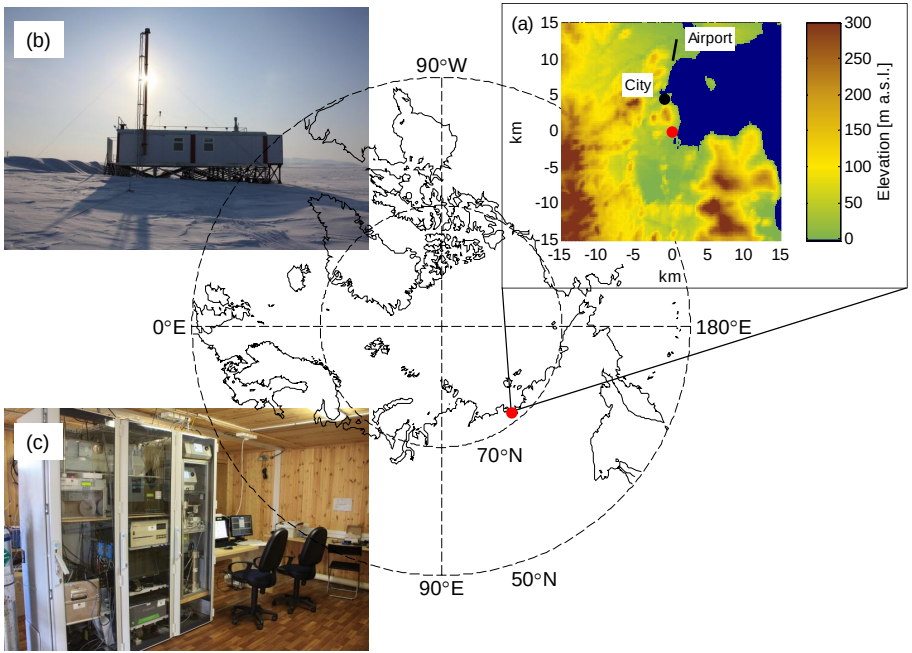

Figure 1. Location of the Tiksi measurement station. **(a)** Topographic map insert (United States Geological Survey, 2015) of the surroundings of the measurement site (station indicated by a red dot). **(b)** The station as seen from outside. **(c)** The station interior.

ACPD
15, 18109–18149, 2015

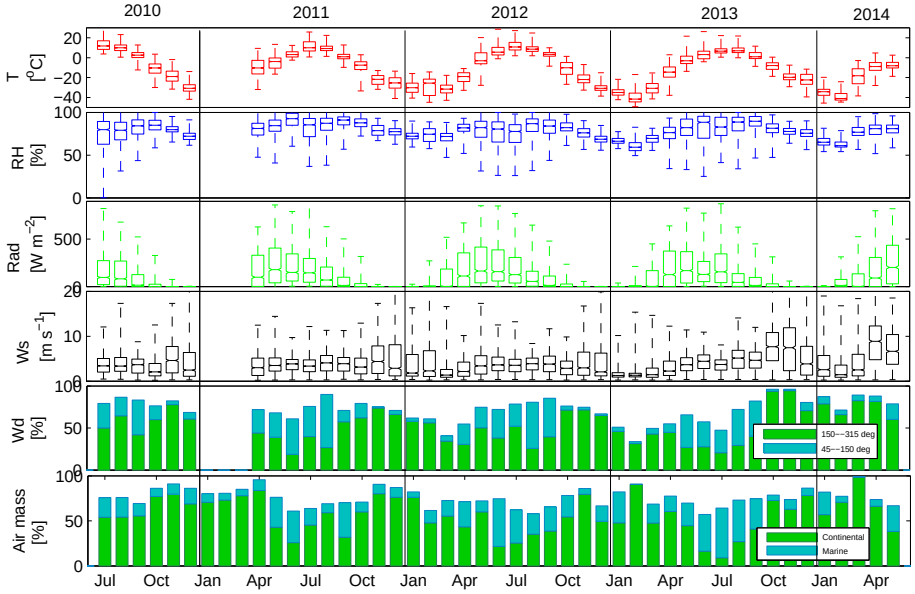

Figure 2. Summary of the meteorological conditions during the measurements. The panels 1–4 (from top to down) depict temperature, relative humidity (RH), global radiation and wind speed, depicted with bars showing extremes, quartiles and median values for each of the parameters monthly. Wind direction (panel 5) is expressed as percents from sector 45–315° (marine sector) and from 150–315° (continental sector), leaving out the sector defined as polluted. Air mass origin (panel 6) is presented as percents of continental (≥ 70 % during preceding 120 h) and marine (≥ 70 % during preceding 120 h) air masses, leaving out the mixed air masses. Also note that RH is expressed as the ratio of the water vapor pressure to the saturation water vapor pressure over water that is a meteorological convention. In freezing winter conditions, condensation will occur at a lower relative humidity than 100 % (over water) when the vapor is saturated against ice.

ACPD
15, 18109–18149, 2015

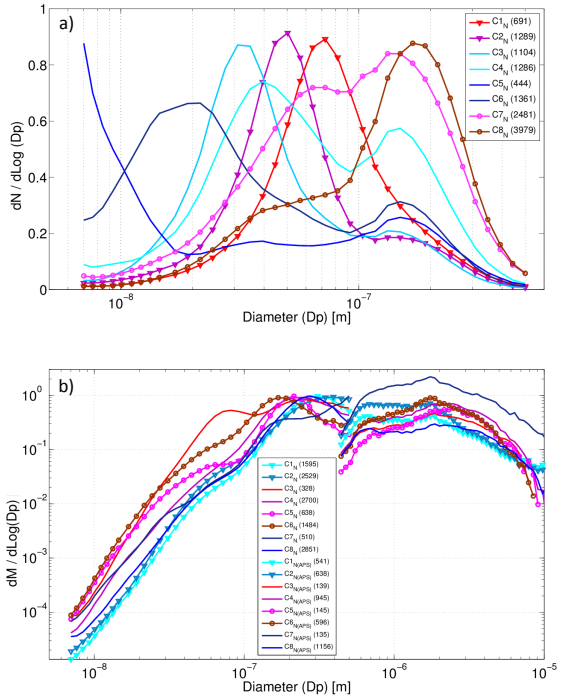

Figure 3. Particle number size distributions for different clusters (no. 1–8) of normalized **(a)** number and **(b)** mass size distributions. *x* axis shows the particle diameters (m), *y* axis the lognormal size distributions normalized with the distribution of maximum concentration in each cluster (no units). In **(a)**, the reddish colors indicate the four most continental cluster types, as bluish the most marine. In **(b)**, the reddish colors indicate the four cluster types of warmest average temperatures, as bluish those of most cold. Triangles mark the two clusters of highest average total **(a)** number and **(b)** mass concentrations and circles those of lowest (in **(b)**; based on DMPS only). In legend the number of cases for each cluster is given in parenthesis. In **(b)** the APS mass size distributions belonging to each of the clusters are presented with separated lines (when available).

ACPD
15, 18109–18149, 2015

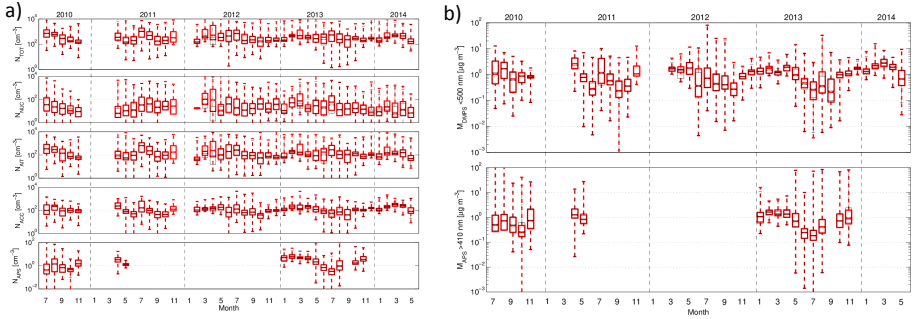

Figure 4. (a) Temporal variability of aerosol total (7–500 nm), nucleation mode (7–25 nm), Aitken mode (25–100 nm), accumulation mode (100–500 nm) and coarse mode (> 410 nm) number concentration, from top to bottom correspondingly. **(b)** Temporal variability of aerosol total (7–500 nm) and coarse mode (> 410 nm) mass concentration, from top to bottom correspondingly. Red bars show quartiles for each month of data available and whiskers the extremes. Black bars are calculated equally but excluding data measured when wind speed was $< 2\,\mathrm{m\,s^{-1}}$. Dotted black lines mark the change of a year.

ACPD
15, 18109–18149, 2015

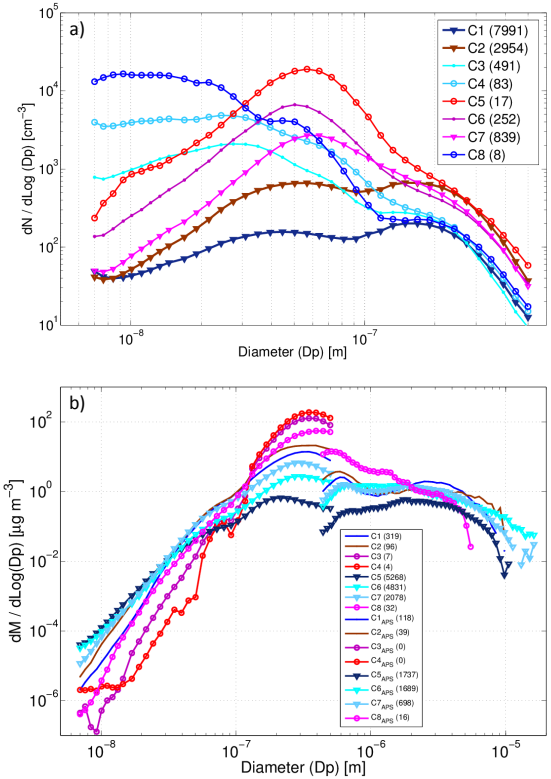

Figure 5. Average particle **(a)** number and **(b)** mass size distributions for different clusters (no. 1–8). In **(a)** the reddish colors indicate the four most continental cluster types, as bluish the most marine. In **(b)** the reddish colors indicate the four cluster types of warmest average temperatures, as bluish those of most cold. Triangles mark the three most common cluster types found and circles the most rare ones. In legend the number of cases for each cluster is given in parenthesis. In **(b)** the APS mass size distributions belonging to each of the clusters are presented with separated lines (when available).

ACPD
15, 18109–18149, 2015

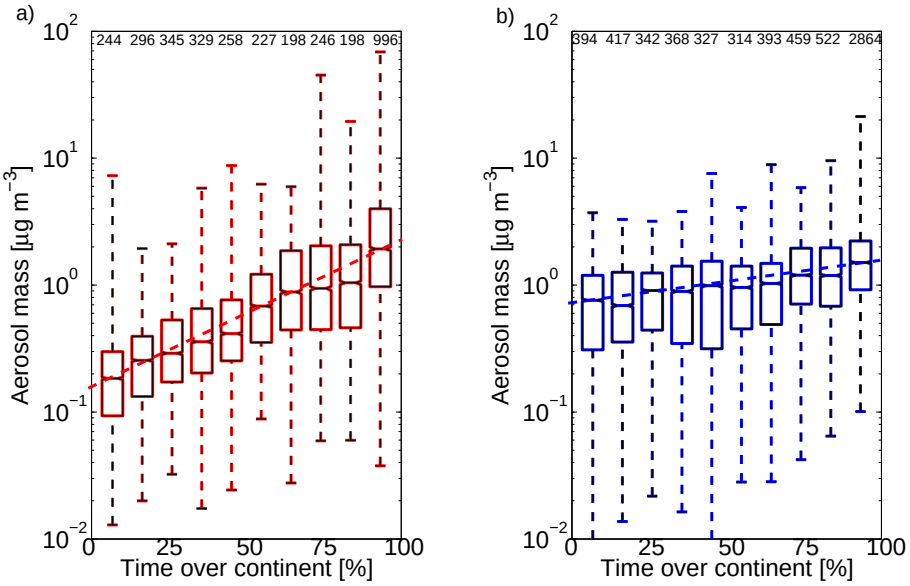

Figure 6. Aerosol total mass (≤ 500 nm) vs. percentage of time the air mass spent over continental areas over the last 120 h. Median mass concentration around each back-trajectory (for every 3 h) was used in calculations. In left panel **(a)** in red are depicted the data measured in temperatures ≥ 0 °C and in right panel **(b)** those in temperatures < 0 °C. Boxes show the quartiles with whiskers extending to extreme data points. On top of each box is the number of cases used in calculations. Dash red and blue lines are added to guide the eye.

ACPD
15, 18109–18149, 2015

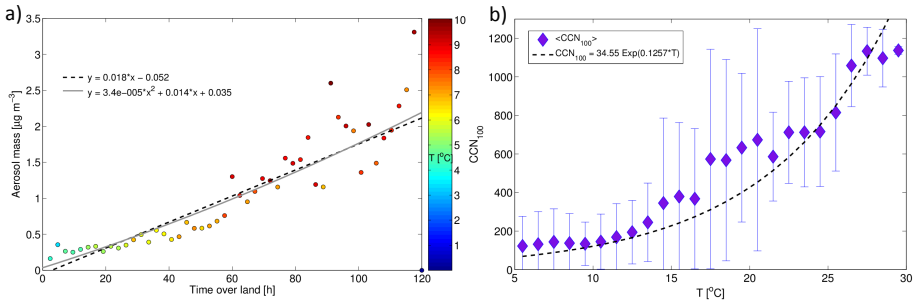

Figure 7. (a) Average aerosol total mass (≤ 500 nm) as a function of air mass time spent over land. Color indicates the average temperature for each point. Dashed black line shows the linear fit and and grey line the quadratic fit, along with the fitting equations obtained. **(b)** Average CCN_{100} concentration (diamonds) and bars presenting its standard deviation, as a function of measurement temperature with an exponential fit to the data ($R_2 = 0.97$).

ACPD
15, 18109–18149, 2015

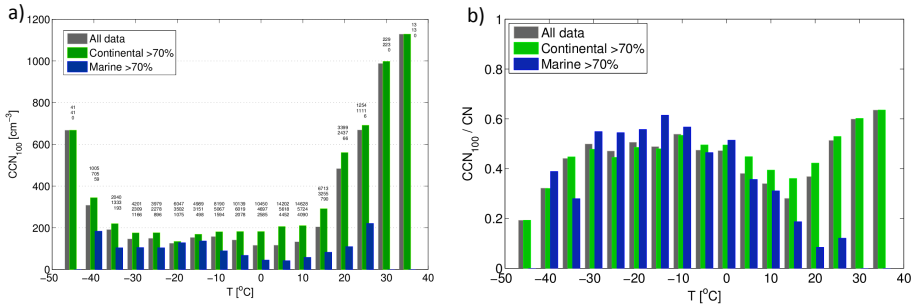

Figure 8. (a) Average CCN_{100} concentration as a function of measurement temperature. Different bars present cases calculated using all data (dark grey), continental data (green) and marine data (blue). The numbers on top of each bar show the amount of DMPS data available for each total, continental and marine cases, from top to down, which is equal also for panel **(b)**. **(b)** Average CCN_{100} to CN ratio as a function of measurement temperature. Different bars present cases calculated using all data (dark grey), continental data (green) and marine data (blue).

ACPD
15, 18109–18149, 2015

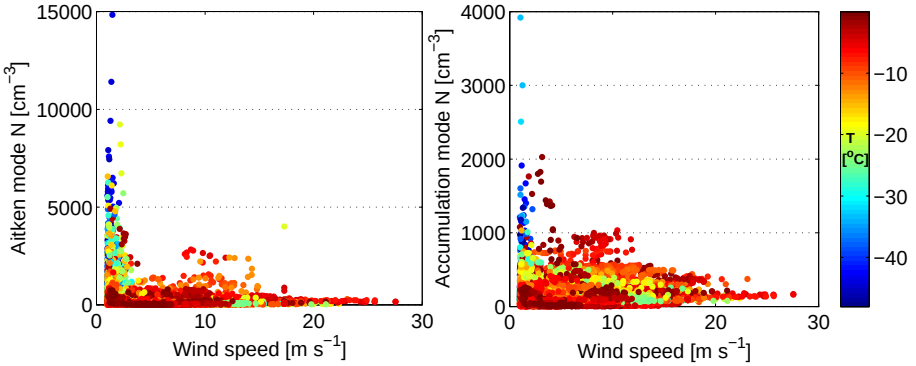

Figure 9. Dependence of Aitken (25–100 nm) and accumulation (100–500 nm) mode concentrations on wind speed for days of negative temperatures. Colorbar shows the range of temperatures for each measured point.

ACPD
15, 18109–18149, 2015